Research Square

Preprints are preliminary reports that have not undergone peer review.
They should not be considered conclusive, used to inform clinical practice,
or referenced by the media as validated information.

WBP2/YAP1 complex governs miR-133b maturation and ovarian development in teleosts

Jiayu Zhou
Southern Marine Science and Engineering Guangdong Laboratory-Zhanjiang
Qianwen Min
Southern Marine Science and Engineering Guangdong Laboratory-Zhanjiang
Xin Yi
Southern Marine Science and Engineering Guangdong Laboratory-Zhanjiang
Bi Huang
Southern Marine Science and Engineering Guangdong Laboratory-Zhanjiang
Meiqi Lv
Southern Marine Science and Engineering Guangdong Laboratory-Zhanjiang
Ruojing Li
Southern Marine Science and Engineering Guangdong Laboratory-Zhanjiang
Na Zhao
Southern Marine Science and Engineering Guangdong Laboratory-Zhanjiang
Bo Zhang
zb611273@163.com

Southern Marine Science and Engineering Guangdong Laboratory-Zhanjiang

Research Article

Keywords: WBP2, YAP, miR-133b, miRNA biogenesis, teleosts, ovarian development

Posted Date: October 14th, 2026

DOI: https://doi.org/10.21203/rs.3.rs-11080484/v1

License: This work is licensed under a Creative Commons Attribution 4.0 International License.
Read Full License

Additional Declarations: No competing interests reported.

Abstract

Impaired miRNA biogenesis causes abnormal ovarian development in teleost fish. Nevertheless, how the WBP2-YAP1 signalling module regulates miRNA maturation and gonadal endocrine homeostasis remains poorly understood. In this study, we combined multiple experimental approaches, including cross-linking mass spectrometry (XL-MS), GST pull-down assays, molecular docking, cell-based functional perturbation, small-RNA sequencing, quantitative real-time PCR, and gonadal histomorphological assessment. Using greater amberjack (*Seriola dumerili*) and large yellow croaker (*Larimichthys crocea*) as model species, we investigated the cooperative function of WBP2-YAP1 in controlling miR-133b biogenesis during ovarian maturation. Structural analyses identified key interfacial residues that mediate physical interactions among WBP2, YAP1, and DGCR8. These results confirm that WBP2 serves as a molecular scaffold to recruit YAP1 to the DGCR8-containing miRNA-processing microprocessor. Functional assays demonstrate that *wbp2* and *yap1* work synergistically to promote miR-133b maturation, and simultaneous silencing of both genes generates a combined repressive molecular effect. Our results reveal a conserved bidirectional feedback circuit formed by miR-133b and *wbp2/yap1* in the teleost ovary. Pathway enrichment analyses show that genetic disruption of *wbp2* and *yap1* reshapes multiple signalling cascades associated with estrogen biosynthesis and oocyte growth, including the Hippo, MAPK, cAMP, and GnRH pathways. Silencing *wbp2* shifts ovarian phenotypes toward the late vitellogenic stage, consistent with accelerated ovarian maturation. Pharmacological treatment with exogenous E_2 and tamoxifen further demonstrates tissue-specific activation of this regulatory axis. In female gonads, E_2 triggers an autoregulatory negative-feedback loop: it induces miR-133b to suppress estrogen-synthesis-related transcripts. By contrast, tamoxifen elicits a transcriptional pattern opposite to E_2. In summary, this work describes the cooperative *wbp2-yap1*-dependent mechanism that controls miR-133b maturation and estrogen homeostasis. It extends the known bidirectional closed-loop regulatory model between miR-133b and *wbp2*, and provides key mechanistic insights into post-transcriptional networks governing teleost gonadogenesis.

1. Introduction

Gonadal development of teleosts constitutes a pivotal research frontier spanning aquaculture biotechnology and developmental biology. Estrogen signalling acts as a highly conserved master regulator that governs vertebrate gonadal differentiation and maturation (Devlin and Nagahama 2002; Zohar 2021; Nicol et al. 2022; Zhang et al. 2017). However, the miRNA-dependent epigenetic circuitry that modulates ovarian estrogen biosynthesis has not been fully delineated in teleost species.

MicroRNAs serve as essential epigenetic modulators of teleost gonadogenesis, governing folliculogenesis and ovarian maturation through post-transcriptional repression of core components in the estrogen biosynthetic axis. To date, comprehensive characterizations connecting miR-133b activity with estrogen signaling and gonadal maturation remain scarce in bony fish. Critically, the upstream regulatory framework that controls miR-133b biogenesis is yet to be fully resolved. Functional evidence confirms that miR-133b directly engages effector genes linked to steroidogenesis, including *tagln2, foxl2,*

cyp19a1a and *wbp2*, to program gonadal developmental trajectories. Ma et al. (2021) demonstrated that ovarian miR-133b targets *tagln2*, which remodels the transcriptional output of *foxl2* and *cyp19a1a* in tilapia steroidogenic cascades (Ma et al. 2021). Earlier work confirmed direct repression of *foxl2* by miR-133b (Dai et al. 2013). Rather than regulating canonical ER-dependent transcription (Hammes and Levin 2007), *Foxl2* modulates estrogen signalling via non-genomic transcriptional circuits (Kim et al. 2009). In olive flounder and tilapia, Foxl2 functions as a transcriptional activator for *cyp19a1a* and promotes de-novo estrogen biosynthesis (Wang et al. 2007; Yamaguchi et al. 2007). Among known downstream mediators of the miR-133b-steroidogenic module, the functional targeting between miR-133b and *wbp2* has only recently received systematic experimental validation in marine aquaculture fish (Zhou et al. 2025).

Working with greater amberjack (*Seriola dumerili*), Zhou et al. (2025) applied dual-luciferase reporter assays, RNA-FISH and in-vivo agomir-antagomir functional manipulation. Their experiments validated that miR-133b-3p directly binds the 3'-UTR of *wbp2* and represses *wbp2* at the post-transcriptional level. Co-localisation of miR-133b-3p and *wbp2* was detected in ovarian stromal cells. In-vivo overexpression of miR-133b-3p reduced *wbp2* transcript abundance and repressed multiple steroid-related transcripts (*esrra, foxl2a, cox2*), ultimately suppressing ovarian estrogen biosynthesis. This post-transcriptional targeting mechanism is evolutionarily conserved across teleost lineages.

These previous studies have described only a one-way inhibitory axis: miR-133b represses *wbp2*. The canonical model of miRNA-mediated target repression is well-characterized. By comparison, target-driven reverse miRNA regulation — in which target genes themselves control miRNA maturation or turnover — has been reported in only a small number of cases, with limited effector proteins experimentally confirmed for such feedback functions. Primary miRNA maturation is carried out by the core microprocessor complex composed of Drosha, DGCR8, DDX5 and DDX17. Independent functional studies show that both WBP2 and YAP interact physically with this complex to tune miRNA production. As an oncogenic effector, WBP2 participates in downstream signalling of Wnt, EGFR and Hippo pathways (Tabatabaeian et al. 2020). WBP2 binds DGCR8–DDX5 sub-complexes, blocks pri-miRNA-to-pre-miRNA processing, and causes global repression of cellular miRNA biogenesis (Tabatabaeian et al. 2021a). Upon nuclear translocation, Hippo effector YAP associates with microprocessor subunit DDX17 and inhibits miRNA production in a cell-density-dependent manner. Cytoplasmic retention of YAP greatly weakens this repressive activity (Mori et al. 2014). Combined structural-functional data demonstrate that YAP interacts with WBP2 through WW–PPXY motif pairing, and this interaction synergistically enhances PR- and ER-driven transcription. Importantly, YAP-dependent ER transactivation strictly requires WBP2 co-expression (Dhananjayan et al. 2006; Sudol et al.1995). Although their physical interaction relies on WW–PPXY recognition, the protein domains responsible for microprocessor recruitment are spatially distinct. This feature prevents competitive binding and enables cooperative miRNA regulation (Tabatabaeian et al. 2021a). A few isolated examples have illustrated target-driven reverse miRNA control. For instance, CAT-1 interacts with miR-122 and facilitates its maturation (Bose and Bhattacharyya 2016). Within teleost systems, existing evidence only supports unidirectional repression of *wbp2* by miR-133b (Zhou et al. 2025). Whether *wbp2* can in turn

regulate miR-133b maturation via the core microprocessor complex remains untested. Prior publications have studied *wbp2* or *yap* individually. They have not addressed how the WBP2–YAP complex engages the miRNA-processing machinery to sustain miR-133b biogenesis and establish reciprocal feedback together with miR-133b-mediated *wbp2* repression. The complete signalling cascade linking WBP2–YAP-driven miR-133b maturation to ovarian physiological outputs has not been described, which represents an important unresolved research gap.

The present study focuses on this regulatory axis of teleost ovarian development. We aim to investigate how *wbp2* cooperates with *yap1* to exert reverse control over miR-133b maturation through the microprocessor complex. We further characterise the reciprocal regulatory circuit formed by miR-133b and *wbp2* that modulates estrogen biosynthesis and gonadogenesis. Findings from this work will expand the epigenetic knowledge base for teleost gonadal maturation, improve our understanding of bidirectional crosstalk between non-coding RNAs and target transcripts, and broaden the inventory of known gene-regulatory networks governing vertebrate reproductive development.

2. Materials and Methods

This study adhered to the ARRIVE and PREPARE guidelines for animal experimentation. All animal experimental protocols were reviewed and formally approved by the Animal Ethics Committee of the Southern Marine Science and Engineering Guangdong Laboratory (Zhanjiang) (approval no. ZJW202307181).

2.1. Plasmid Construction

2.1.1. PCR Amplification and Gel Purification of Target *yap1* and *dgcr8* DNA Fragments

Healthy 1-year-old greater amberjack (*Seriola dumerili*), sourced from a commercial aquaculture farm in Zhangzhou, Fujian Province, were maintained in recirculating seawater tanks at 26°C under a natural photoperiod (Fernández-Montero et al. 2018). During acclimation, water temperature was held at 26°C and dissolved oxygen was kept ≥ 5 mg/L with routine feeding; fish were subjected to a 24 h fasting regime prior to dissection and sampling. Following anesthesia with 50 mg/L MS-222, liver tissues were harvested from three biologically independent greater amberjack individuals (body length, 50 cm; body mass, 1 kg) for RNA extraction and subsequent reverse transcription. PCR amplification was performed in a 50 μL reaction mixture comprising 22 μL ddH_2O, 25 μL TaKaRa Mix, 1 μL cDNA template, and 1 μL each of the forward and reverse primers. The thermal profile included an initial denaturation at 95°C for 5 min, 35 cycles of denaturation (95°C, 10 s), annealing (58°C, 5 s) and extension (72°C, 20 s or 51 s), followed by a final extension at 72°C for 5 min (Celie et al. 2016; Yan et al. 2022). Amplified products were resolved via agarose gel electrophoresis (115 V, 400 mA, 25–30 min), using a 2000-bp or 10000-bp DNA ladder as the molecular size reference. The vector and target-gene amplicons were separately gel-purified with an agarose gel DNA recovery kit (Tiangen, China), and DNA concentrations were

quantified thereafter. Gene-specific primers for target gene amplification were commercially designed and synthesized by Sangon Biotech (Shanghai) Co., Ltd., with sequences listed in Table S1.

2.1.2. Assembly of Recombinant Constructs Using Homologous Recombination-Mediated Cloning

The purified pET-30a(+) plasmid backbone (supplied by Nanjing Zhongding Biotechnology Co., Ltd.) and target-gene insert were mixed at an optimized molar ratio in a final reaction volume of 10 μL. The loading amounts of backbone and insert were calculated based on gel-purified DNA concentrations; for reference, 20 ng of DNA was applied for a 2000-bp fragment. Thereafter, 1 μL of homologous recombinase and 2 μL of the corresponding reaction buffer (Vazyme Biotech Co., Ltd., Nanjing, China) were added, and the assembly mixture was incubated at 37°C for 30 min. A 10-μL aliquot of the assembly product was transformed into 100 μL DH5α competent cells. The transformation mixture was incubated on ice for 30 min, subjected to heat shock at 42°C for 90 s, and chilled on ice for another 5 min. One milliliter of antibiotic-free LB broth was supplemented, followed by incubation at 37°C for 1 h. Following centrifugal enrichment, 100 μL of the cell suspension was spread onto KanR-selective LB agar plates and incubated for approximately 16 h (Celie et al. 2016; Yan et al. 2022). Individual colonies were picked and screened via colony PCR to obtain positive recombinants. Validated bacterial cultures were submitted to Sangon Biotech (Shanghai) Co., Ltd. for Sanger sequencing. Sequence-confirmed positive recombinants served as constructs for downstream recombinant protein expression assays.

2.2. Induction and IMAC Purification of Recombinant His-Tagged Fusion Proteins

2.2.1. Transformation of Recombinant Constructs into *Escherichia coli* Arctic-Express Competent Cells

One microliter of plasmid DNA was mixed with 100 μL competent cells and incubated on ice for 20 min. The sample was then subjected to a 90-s heat-shock treatment at 42°C, immediately chilled on ice for 5 min, and supplemented with 600 μL LB broth. The cell suspension was incubated at 37°C with shaking at 220 rpm for 1 h. Following centrifugation, the whole cell pellet suspension was plated onto LB agar plates containing 50 μg/mL kanamycin (Kan). The plates were incubated inverted overnight at 37°C (Bjerga and Williamson 2015; Sohn et al. 2025).

2.2.2. IPTG-Mediated Induction of Recombinant Fusion Protein Expression in *Escherichia coli*

Single colonies derived from transformation plates were inoculated into 3 mL antibiotic-supplemented LB broth (50 μg/mL kanamycin) and cultured overnight at 37°C with orbital shaking at 220 r/min. The overnight culture was diluted 1:100 into 30 mL fresh selective LB medium and incubated under identical conditions until the OD_{600} ranged from 0.6 to 0.8. A 1-mL culture aliquot was pelleted by centrifugation (10 000 r/min, 2 min, room temperature), the supernatant was discarded, and the cell pellet was

resuspended in 100 μL of 1× protein-loading buffer. Isopropyl-β-D-thiogalactopyranoside (IPTG) was supplemented to the remaining bacterial suspension at a final concentration of 0.5 mM, and the culture was incubated for an additional 4 h (37°C, 220 r/min) to trigger fusion-protein expression (Nettleship et al. 2019; Jiang et al. 2023; Supratim Dey et al. 2025). A second 1-mL sample was collected and processed using the same centrifugation-resuspension workflow. The leftover culture was centrifuged at 4 000 r/min for 10 min; the cell pellet was resuspended in PBS and disrupted by sonication. Soluble supernatant and insoluble pellet fractions were recovered independently and resuspended in loading buffer. Protein samples were resolved on 12% SDS-PAGE gels and stained with Coomassie brilliant blue for band detection.

2.2.3. Immobilized-Metal-Affinity Chromatography (IMAC)-Based Purification of Recombinant Fusion Proteins

Recombinant His-YAP1 and His-DGCR8 proteins were subjected to affinity purification using a low-pressure liquid chromatography system. The soluble supernatant was loaded at 0.5 mL/min onto a Ni-IDA-Sepharose Cl-6B resin pre-equilibrated with Ni-IDA Binding-Buffer. Following sample application, the column was rinsed with equilibration buffer at an identical flow rate (0.5 mL/min) until the OD_{280} absorbance of the flow-through stabilized at the baseline. Non-specifically bound contaminants were washed off using Ni-IDA Washing-Buffer (20 mM Tris-HCl, 30 mM imidazole, 0.15 M NaCl, pH 8.0) at 1 mL/min until OD_{280} returned to baseline. Bound recombinant protein was eluted with Ni-IDA Elution-Buffer (20 mM Tris-HCl, 250 mM imidazole, 0.15 M NaCl, pH 8.0) at 1 mL/min, and elution fractions were pooled (Bornhorst and Falke 2000; Lanio et al. 2003). The recovered protein fractions were transferred to dialysis membranes and subjected to overnight dialysis against PBS.

2.2.4. Protein Separation and Detection by SDS-PAGE

An 80-μL aliquot of protein sample was combined with 20 μL of 5× loading buffer supplemented with β-mercaptoethanol, boiled for 10 min, and centrifuged at 12 000 rpm for 10 min prior to loading. A 5-μL volume of the denatured sample was carefully loaded into individual gel wells, and electrophoresis was run at a constant voltage of 80 V. After the bromophenol blue dye front condensed into a distinct line at the stacking-separating gel interface, the voltage was increased to 120 V. Electrophoresis was terminated once the tracking dye reached the bottom edge of the gel (Gallagher S and Sasse J 2001). The gel was stained with rapid protein stain (Aidison) on an orbital shaker with gentle agitation for 10 min. Excess dye was removed by washing with deionized water until a low-background contrast was achieved, and the gel image was captured for record-keeping (Brunelle and Green 2014).

2.3. Generation and Purification of Polyclonal Antibodies

Production and purification of the WBP2 polyclonal antibody were commercially performed by Nanjing Zhongding Biotechnology Co., Ltd. New Zealand white rabbits weighing 2.0–2.5 kg were acclimated for 7 days prior to immunization. Purified antigen (purity ≥ 90%) was emulsified 1:1 (v/v) with complete Freund's adjuvant (CFA) for primary immunization. Each rabbit received 200–400 μg antigen administered by multi-site subcutaneous injection. Subsequent booster injections were given biweekly

with 100 μg antigen emulsified in incomplete Freund's adjuvant (IFA). Serum titers were evaluated by ELISA using blood collected from the ear marginal vein on day 42. Large-volume blood harvesting was performed through carotid venipuncture following the third booster dose. Recovered antiserum was clarified by centrifugation at 10 000 r/min for 10 min at 4°C, and polyclonal immunoglobulins were enriched by Protein A/G affinity chromatography. Final antibody preparations were characterized for purity, concentration and antigen specificity using SDS-PAGE, A_{280} ultraviolet spectrophotometry and Western blot assays, respectively (Thong B et al. 1985; Yang Xh et al. 2020; Zhu L et al. 2021).

2.4. Pull-Down Assays

0.5 mL of well-resuspended glutathione resin slurry was split into two centrifuge tubes for control and experimental assays. Following pre-chilled buffer washing, the control resin was incubated with 1 mg of recombinant GST protein, while the experimental resin received 1 mg of purified GST-tagged fusion protein at 4°C for 60 min. Unbound proteins were discarded after centrifugation, and each resin pellet was washed three times with GST wash buffer. Both sets of beads were then incubated with 1 mg of purified His-tagged target protein overnight at 4°C using an end-over-end rotator to enable protein-protein interaction (Kim and Hakoshima 2019). Post-reaction centrifugation was performed, and the washing cycle was repeated to remove non-specific interactors. Captured protein complexes were eluted with glutathione elution buffer, and recovered eluates were subjected to SDS-PAGE and immunoblotting for interaction validation (Smith and Johnson 1988; Louche et al. 2017). Recombinant proteins (GST-tagged control, GST-YAP1, GST-DGCR8 and His-WBP2) applied in this study were commercially produced by Nanjing Zhongding Biotechnology Co., Ltd.

2.5. Analysis by Chemical Cross-Linking-Mass Spectrometry (XL-MS)

DSS-cross-linked protein samples were proteolytically digested into short peptides with trypsin or GluC, yielding a peptide pool that preserved covalent cross-linking signatures. Digested peptides were subjected to liquid chromatography-tandem mass spectrometry (LC-MS/MS). MS1 survey scans recorded the intact precursor masses of cross-linked peptide species. Peptide fragmentation for cross-link site annotation was achieved in the MS2 step via collision-induced dissociation (CID) or higher-energy collisional dissociation (HCD). The chemical cross-linking mass spectrometry (XL-MS) experiment was commercially performed by Beijing BTP Biotechnology Co., Ltd. Cross-linking datasets were computationally processed, and inter-protein cross-linked pairs were assigned using the p-link workflow. Cross-linked residues were localized by combining the diagnostic high-molecular-weight signature of cross-linked peptides and site-specific MS/MS fragment evidence. The resulting cross-linking information was assembled into a protein-protein interaction network and residue-resolved binding interface map (Jones et al. 2019; Wang et al. 2022; Chen et al. 2022).

2.6. *In silico* Prediction of Protein Interaction Interfaces via AlphaFold-Multimer

Three-dimensional complex modelling of WBP2 (XP_022598504.1), YAP1 (XP_022617223.1) and DGCR8 (XP_022610203.1) was performed via the web-based AlphaFold-Multimer server. Amino-acid sequences were imported to generate quaternary-structure predictions for the ternary protein assembly. Predicted models were filtered using confidence cut-offs of pLDDT ≥ 70 and DockQ ≥ 0.23(Basu and Wallner 2016; Tunyasuvunakool et al. 2021). Inter-protein binding interfaces and functionally critical residues were characterised on the basis of interatomic distances, interface contact areas and residue-resolved interaction fingerprints. PyMOL was employed for graphic rendering of intermolecular contact regions and evolutionarily conserved hot-spot residues (Yu et al. 2023).

2.7. Preparation of Overexpression Constructs and siRNA Reagents

Custom siRNA reagents and gene-specific overexpression constructs targeting *wbp2* (XM_022742783.1) and *yap1* (XM_022761502.1) were commercially synthesized by GenePharma Co., Ltd. (Suzhou, China) (Zhang et al. 2024). Sequences for target-gene cloning primers and siRNA oligonucleotides are listed in Table S1. The pcDNA3.1(+) backbone was linearized by double digestion with NheI and XhoI (Fermentas); linear vector fragments were gel-purified after agarose electrophoretic separation. Purified target gene inserts were assembled with the linearized pcDNA3.1(+) vector through homologous recombination using the ClonExpress® Entry One Step Cloning Kit (Vazyme Biotech Co., Ltd., Nanjing, China). Recombinant mixtures were transformed into *E. coli*, and transformants were selected on ampicillin-supplemented LB solid medium. Miniprep-purified plasmids were preliminarily validated by restriction digestion (NheI/XhoI), followed by Sanger sequencing to confirm sequence accuracy. A vacant pcDNA3.1-GFP empty vector was generated synchronously to serve as a negative control for downstream functional assays (Yin et al. 2026).

2.8. Maintenance of Cultured Cells

Human embryonic kidney (HEK-293T) cells were maintained in high-glucose Dulbecco's modified Eagle's medium (DMEM) containing 10% fetal bovine serum (FBS) and 1% penicillin-streptomycin solution. Cultures were incubated at 37°C under a humidified atmosphere of 5% CO_2. Upon reaching 80%–90% confluence, adherent cells were trypsinised and passaged. Exponentially growing cells with favourable cellular status and sterility were harvested for downstream functional assays (Boroda et al. 2022; Li et al. 2023; Jo and Nam 2025).

2.9. Transfection of siRNA and Overexpression Constructs in Cultured Cells

Cells were passaged into 24-well plates 24 h prior to transfection. On the day of treatment, growth medium was replaced with serum-reduced medium (1 mL/well). Three hours later, pre-formed Lipomaster 3000-DNA-T3000 Enhancer complexes were added drop-wise to each well, and plates were swirled gently to ensure uniform distribution. At 24 h post-transfection, the medium was aspirated; cells

were washed twice with PBS and replenished with fresh serum-reduced medium (1 mL/well) before microscopic observation (Dalby et al. 2004).

Complex preparation per well: One sterile 1.5 mL microcentrifuge tube contained 25 μL Opti-MEM mixed with 1.5 μL Lipomaster 3000 Reagent. A second tube was prepared with 25 μL Opti-MEM, 0.5 μg plasmid DNA and 1 μL T3000 Enhancer Reagent. The DNA-enhancer mixture was added dropwise to the lipid solution, mixed gently, and incubated at room temperature for 10 min to allow complex formation. siRNA transfection was performed following the same protocol, with the exclusion of T3000 Enhancer Reagent (Jiang et al. 2021).

2.10. micro RNA sequencing

Total RNA was isolated from six experimental groups of transfected cells: *yap1* single knockdown (Y0), *wbp2* single knockdown (W0), *wbp2*/*yap1* double knockdown (W0Y0), *wbp2* knockdown with yap1 overexpression (W0Y1), *wbp2* overexpression with yap1 knockdown, and the negative control (NC). RNA integrity and purity were assessed. Validated RNA samples were subjected to small-RNA library construction followed by high-throughput miRNA sequencing. Raw sequencing data underwent quality control, adapter removal and low-quality read filtering to generate clean reads. Processed clean reads were aligned against the reference genome to enable miRNA annotation and differential expression profiling (Zhao et al. 2021, 2023). Candidate differentially expressed miRNAs were retrieved, and functional enrichment analysis was conducted for their predicted target genes (Presslauer et al. 2017).

2.11. Quantitative Real-Time PCR (qPCR)

Total RNA was isolated from cell samples across all groups and reverse-transcribed to generate cDNA templates. Quantitative real-time PCR (qRT-PCR) was performed using the SYBR Green-based fluorescent dye system. Target gene expression values were normalized against an endogenous reference gene, and relative transcript abundance was quantified via the $2^{-\Delta\Delta Ct}$ algorithm (Livak and Schmittgen 2001; Zhao et al. 2025; Ba et al. 2025). Gene-specific primers used for qRT-PCR validation were commercially designed and synthesized by Sangon Biotech (Shanghai) Co., Ltd., with primer sequences listed in Table S1. Brain and gonadal tissues collected in Section 2.14 were processed identically. *β-actin* was adopted as the reference gene for mRNA qPCR normalization, with its primer pair designed from the conserved coding region of large yellow croaker *actb* and experimentally validated. U6 snRNA served as the reference gene for miRNA qPCR normalization (Liu et al. 2019).

2.12. In-vivo siRNA Microinjection Assay

Cultured large yellow croaker (*Larimichthys crocea*) were sourced from Hengxing Southern Marine Science and Technology Co., Ltd., China. Six healthy large yellow croaker (body length: 13 cm; body weight: 60–100 g) were randomly assigned to two experimental groups (n = 3 biologically independent fish per group): a negative-control group (NC) and a *wbp2* siRNA-treated group (W0). Anaesthesia was performed using eugenol. Fish were intraperitoneally injected at a dose of 1 μg/g body weight. The NC group received an equal volume of sterile PBS, whereas the W0 group was administered siRNA with a

final concentration of 1 μg/μL (Pan et al. 2021). All experimental animals were maintained in independent aquaria. At 4 h post-injection, fish were anesthetized using 50 mg/L MS-222. Ovarian tissues were excised via dissection and immediately fixed in 4% PFA for subsequent paraffin embedding and histological sectioning.

2.13. Histological Analysis of Ovarian Tissue

Fixed ovarian tissue specimens were subjected to serial graded ethanol dehydration using a tissue processor (JJ-12 J, Wuhan Junjie Electronics Co., Ltd.), followed by embedding in molten paraffin. Trimmed paraffin blocks were sectioned at 4 μm using a rotary microtome (RM2016, Leica Biosystems). Sections were stained with hematoxylin and eosin (H&E), and histological images were acquired under an optical microscope with Leica Application Suite X (Qu et al. 2025).

2.14. In-vivo Hormone Administration Assay

Thirty healthy large yellow croaker (body length: 13 cm; body weight: 60–100 g) were randomly assigned to three experimental groups (n = 10 biologically independent fish per group, balanced sex ratio): vehicle control group, 17β-estradiol (E2)-treated group, and tamoxifen-treated group. Stock solutions of E2 and tamoxifen (20 mg/mL) were dissolved in dimethyl sulfoxide (DMSO) and further diluted using sterile corn oil to yield a working concentration of 5.2 mg/mL (Abdollahpour et al. 2025). The control group received an equivalent volume of sterile corn oil as the vehicle. Following eugenol-mediated anaesthesia, all individuals were intraperitoneally injected at a dosage of 1 μL/g body weight. Experimental fish were maintained in independent aquaria. At 4 h post-injection, fish were anesthetized using 50 mg/L MS-222. Brain and gonadal tissues were subsequently excised and immediately flash-frozen in liquid nitrogen for downstream molecular biological analyses (Shi et al. 2022).

2.15. Statistical analysis

qRT-PCR data were presented as the mean ± standard deviation (SD) of three technical replicates per sample. One-way ANOVA followed by Tukey's HSD post-hoc test (SPSS 25.0) was applied to assess intergroup differences, and the threshold for statistical significance was set at $p < 0.05$ (Li et al. 2025).

3. Results

3.1. Production, Purification and Immunological Characterization of Recombinant Fusion Proteins

SDS-PAGE analysis identified distinct bands corresponding to the predicted molecular masses of His-WBP2, GST-YAP1 and GST-DGCR8 upon IPTG induction; no visible target products were present in uninduced bacterial lysates, thus verifying the expression of all three recombinant proteins (Fig. 1A-a, 1B-a, 1C-a). Ni-IDA affinity-purified His-WBP2 yielded a dominant single band in SDS-PAGE (Fig. 1A-b). Coomassie staining and immunoblot analysis further validated the high purity and specific antigenicity of the recovered His-WBP2 (Fig. 1A-c, 1A-d). Likewise, glutathione-affinity enrichment generated

homogenous, high-purity GST-YAP1 and GST-DGCR8 fusion proteins (Fig. 1B-b, 1C-b). Agarose gel electrophoresis confirmed that the inserted fragments within recombinant plasmids pET-His-YAP1 and pET-His-DGCR8 were in agreement with the designed sizes (Fig. 1D-a, 1D-b). Final SDS-PAGE assessment of purified His-YAP1, His-WBP2 and His-DGCR8 showed well-resolved monodisperse bands with negligible impurities, indicating favourable protein purity (Fig. 1D-c).

3.2. Validation of WBP2-YAP1 and WBP2-DGCR8 protein interactions and characterization of their binding sites

GST pull-down assays detected specific His-WBP2 immunoreactive bands in the GST-YAP1 and GST-DGCR8 pull-down fractions, while no target band was recovered from the GST-alone control. These data confirmed the direct binary interactions between WBP2 and YAP1, as well as between WBP2 and DGCR8 (Fig. 2A). Input controls verified equivalent protein loading across all experimental groups.

Molecular docking simulations predicted hydrogen-bonding contacts between WBP2 and YAP1 mediated by HIS207, THR212 and PRO253 (Fig. 2B-a). The WBP2-DGCR8 interface was constituted by SER10, ASP26 and LYS715 (Fig. 2B-b). Ternary-complex docking illustrated that WBP2 engages YAP1 and DGCR8 concurrently to form a stable supramolecular assembly; a discrete contact surface was additionally predicted at the YAP1-DGCR8 interface (Fig. 2B-c).

XL-MS recovered abundant diagnostic cross-linked-peptide fragment ions for the DGCR8-WBP2 complex, substantiating their covalent cross-linking (Fig. 2C-a). Restraint-driven structural modelling pinpointed LYS-681 as a pivotal residue within the DGCR8-WBP2 binding pocket (Fig. 2C-b). Reciprocal cross-linking datasets independently corroborated these contact sites (Fig. 2C-c), with structural restraints mapping an intermolecular cross-link spanning WBP2 LYS-47 and DGCR8 LYS-596 (Fig. 2C-d). Characteristic cross-linking signatures were likewise recovered for the WBP2-YAP1 complex (Fig. 2C-e), defining a cross-linkage connecting WBP2 MET-1 to YAP1 LYS-136 (Fig. 2C-f).

3.3. Small-RNA-seq uncovers miRNA expression signatures across distinct experimental treatments

Biotype classification of sequenced sRNAs (Fig. 3A) demonstrated largely conserved sRNA composition across experimental cohorts. The relative abundance of functionally annotated sRNA species (miRNA, rRNA, tRNA) remained stable throughout treatments, with miRNAs constituting a dominant annotated fraction, which suggests robust enrichment of functional small-RNA populations within our sequencing dataset. Size profiling (Fig. 3B) showed that sRNA reads were predominantly distributed between 21–23 nt, peaking at 22 nt — a size distribution characteristic of canonical mature miRNAs, verifying high-quality sequencing output.

Short Time-series Expression Miner (STEM) analysis was deployed to deconvolve dynamic miRNA trajectories across treatments (Fig. 3C), yielding multiple statistically significant co-expression modules. Module 1 (225 miRNAs, p = 1.2E-45) underwent an initial decline followed by expression restoration.

Module 5 (168 miRNAs, *p* = 2.4E-16) presented an oscillatory expression signature. Module 7 (155 miRNAs, *p* = 3.3E-14) followed a tri-phasic trajectory: an early rise, a subsequent drop and a late-phase recovery.

Principal-component analysis (Fig. 3D) quantified that PC1 and PC2 captured 32.68% and 23.27% of the total transcriptional variance, respectively. Tight intra-group clustering confirmed robust experimental reproducibility. Inter-group segregation was evident: the Y0 and W0 cohorts were well separated from the NC control, while partial overlap was detected between NC and the W0Y0 / W0Y1 treatments.

Hierarchical clustering uncovered divergent expression profiles of differentially expressed miRNAs among treatment groups (Fig. 3E-a, 3E-b). Experimental interference triggered global remodelling of miRNA expression landscapes. A subset of miRNAs retained moderate-to-low basal transcript levels in NC, W0Y0, W0Y1 and W1Y0. By contrast, W0 and Y0 drove robust upregulation of a separate miRNA subset, visualised as extensive contiguous high-abundance red blocks on the heatmap. Clustering based on the full miRNA repertoire yielded expression trends congruent with arm-resolved profiling of 5p/3p isoforms. W0 and Y0 formed a discrete up-regulated transcriptional cluster with expression signatures substantially diverging from the NC control. W0Y0 exhibited a broadly repressive transcriptional profile relative to the control baseline, while W0Y1 and W1Y0 adopted intermediate transcriptional phenotypes between repressed and hyper-activated states.

3.4. Functional enrichment of KEGG pathways for differentially expressed miRNA targets

Pathway enrichment analyses for target genes of differentially expressed miRNAs across all treatment groups are illustrated in Fig. 4A-E. KEGG enrichment of the top 20 pathways for these target genes revealed major significantly enriched pathways, including calcium signaling, parathyroid hormone synthesis, secretion and action, the Hippo signalling cascade, MAPK signalling cascade, Apelin signalling cascade, Wnt signalling cascade, Rap1 signalling cascade, cAMP signalling cascade, AMPK signaling, and phospholipase D cascade.

Target genes regulated by W0 treatment (*wbp2* knockdown) were significantly enriched in focal adhesion, calcium signaling, pathways in cancer, and the parathyroid hormone synthesis, secretion and action cascade (Fig. 4A). Target genes from the W0Y0 cohort (combined *wbp2/yap1* knockdown) exhibited preferential enrichment in the Hippo, MAPK, and Apelin signalling cascades (Fig. 4B).

The Y0 treatment (*yap1* knockdown) shared core enriched pathways with the W0 group, namely focal adhesion, calcium signaling and pathways in cancer; its unique enriched signatures comprised the Wnt, Rap1, cAMP and MAPK signalling cascades (Fig. 4C). Target genes in the W0Y1 comparison group (*wbp2* knockdown + *yap1* overexpression) were significantly enriched in adherens junction, AMPK signaling and axon-guidance pathways (Fig. 4D). In the W1Y0 group (*wbp2* overexpression + *yap1* knockdown), target genes were overrepresented in the phospholipase D cascade, tissue-specific

oncogenic pathways (gastric cancer, breast cancer) and Rap1 signaling. These pathways collectively function in lipid-mediated signal transduction, tumorigenesis and cellular migration (Fig. 4E).

3.5. Assessment of Cell Transfection Efficiency and qRT-PCR Validation

Side-by-side bright-field and fluorescence imaging confirmed stable green fluorescent protein expression in transfected cells with homogeneous fluorescent signals, verifying robust efficient transfection and a valid experimental system (Fig. 5A).Quantitative real-time PCR assays (Fig. 5B) further uncovered divergent transcriptional profiles for pri-miRNA, pre-miRNA and mature miR-133b across experimental cohorts. Relative to the NC controls, pri-miRNA abundance declined significantly following W0, Y0 and W0Y0 stimulation. Conversely, pre-miRNA abundance was significantly increased in the W0 and Y0 groups, while pre-miRNA exhibited strong upregulation in the W0Y1 group and a moderate upward trend in W1Y0, revealing disparate regulatory signatures for these precursor transcripts. Mature miR-133b displayed substantial inter-group variation: its expression was markedly elevated in the W0 group and peaked within the W0Y1 cohort. Although miR-133b abundance in Y0 and W0Y0 was lower than in W0, W0Y1 and W1Y0, both groups displayed higher expression than NC cells. Upon target interference, *wbp2* and *yap1* mRNA abundance decreased significantly in the W0Y0, W0Y1 and W1Y0 treatments, demonstrating efficient knockdown of the two effector genes.

3.6. Histomorphological Observation of Ovarian Tissues Following siRNA Interference in Females

Wild-type ovaries display compact parenchymal architecture, characterized by densely packed oocytes and constricted inter-follicular compartments (Fig. 6A). High-resolution micrographs (Fig. 6C) demonstrate that ovarian follicles are predominantly represented by oocytes arrested at the early-to-mid vitellogenic phase. These oocytes are small in size, with faint eosinophilic cytoplasmic staining and prominent intensely labelled nuclei; fully grown oocytes bearing massive yolk inclusions are rarely detected. In contrast, ovaries from the *wbp2*-knockdown group show a loose oocyte distribution with spacious inter-follicular cavities under low-magnification observation (Fig. 6B). High-power fields capture heterogeneous follicle populations: abundant hypertrophic late-vitellogenic oocytes with eosin-positive cytoplasm loaded with yolk deposits, alongside scattered small previtellogenic oocytes. Such small oocytes feature condensed chromatin, dark-purple haematoxylin-positive nuclei and elevated nucleocytoplasmic ratios. Collectively, comparative histomorphological evidence suggests that *wbp2* silencing is associated with a phenotypic shift towards advanced vitellogenic stages, which is consistent with accelerated ovarian maturation.

3.7. Modulation of estrogen-mediated signaling cascades in gonad and brain tissues upon exposure to exogenous estrogen and its antagonists

Quantitative real-time PCR was used to quantify the transcript levels of miR-133b, core estrogen-biosynthesis genes (*foxl2, cyp19a*), the estrogen receptor gene *esr2a*, and downstream target genes (*wbp2, cox2, yap1*) in gonadal tissues. In female gonads (Fig. 7A), relative to NC controls, E2 significantly elevated miR-133b abundance and repressed *foxl2* and *cyp19a* expression; tamoxifen markedly induced *foxl2, esr2a, cox2* and *yap1*, alongside increased miR-133b levels. In the female brain (Fig. 7B), both E2 and tamoxifen upregulated miR-133b and *foxl2*. Tamoxifen reduced *esr2a* and *wbp2* transcript abundance, whereas E2 increased *esr2a* and *cox2*. In male gonads (Fig. 7C), E2 significantly upregulated miR133b, *foxl2, cyp19a, esr2a, wbp2* and *cox2*. Tamoxifen downregulated miR-133b and *cyp19a*, while increasing *foxl2*. *Yap1* expression was suppressed upon E2 exposure, and tamoxifen significantly enhanced its transcript abundance. In the male brain (Fig. 7D), E2 significantly increased f*oxl2, cyp19a, esr2a* and *cox2* expression and decreased miR133b and *wbp2* levels. Tamoxifen substantially repressed *cyp19a, esr2a, wbp2* and miR-133b. Furthermore, both E2 and tamoxifen significantly induced *foxl2* expression in the male brain. Collectively, exogenous E2 and tamoxifen exert pronounced tissue-specific and sexually dimorphic regulation of miR-133b and estrogen-associated genes, with divergent transcriptional responses elicited by estradiol and tamoxifen across sexes and tissue types.

4. Discussion

This work presents the first structural evidence for the cooperative association of WBP2 and YAP1 with the miRNA-processing machinery. XL-MS pinpointed specific cross-linked residues: Lys-47 in WBP2 paired with Lys-596 in DGCR8, alongside the interface region spanning Met-1 of WBP2 and Lys-136 of YAP1. These residues delineate the intermolecular contact surfaces of the ternary complex. Structurally, these findings clarify how WBP2 and YAP1 cooperate to control miRNA biogenesis. They expand the known functional scope of these two proteins from transcriptional modulation into post-transcriptional miRNA maturation. More notably, our study uncovers a previously undescribed feedback regulatory mechanism. In teleost ovaries, *wbp2* and *yap1* act upstream to promote miR-133b maturation. Prior work has confirmed that miR-133b represses *wbp2* transcripts (Zhou et al. 2025). Together, these two regulatory directions establish a closed reciprocal feedback circuit. Target-driven reverse miRNA regulation has been documented in mammalian systems. In human breast cancer cells, WBP2 binds components of the microprocessor complex and inhibits the conversion of pri-miRNA into pre-miRNA (Tabatabaeian et al. 2021b). Another well-characterized example involves CAT-1. This protein is a direct target of miR-122 and can enhance Dicer1-dependent miR-122 maturation under amino-acid-deprived conditions (Bose and Bhattacharyya 2016). These studies show that only a small set of target proteins can either activate or suppress miRNA maturation. Our results add a new *wbp2*-dependent reverse regulatory pathway operating within the teleost ovarian developmental axis. In this pathway, miR-133b targets *wbp2* to modulate estrogen biosynthesis.

WBP2 represents a WW-domain-bearing adaptor protein that engages interacting partners by recognizing PPXY motifs. As a core transcriptional co-activator within the Hippo signalling cascade, YAP1 also contains multiple WW domains that facilitate a broad spectrum of protein-protein

interactions(Dhananjayan et al. 2006; Sudol et al.). Previous work has confirmed that the WW domain of WBP2 mediates binding to YAP1. This interaction promotes YAP1 nuclear translocation and downstream transcriptional activation. Nevertheless, whether the WBP2-YAP1 complex influences miRNA maturation remained untested. Herein, GST pull-down assays and cross-linking mass spectrometry (XL-MS) validate the direct binding of WBP2 to both YAP1 and DGCR8. Molecular docking further identifies key interfacial residues: His-207, Thr-212 and Pro-253 of WBP2 govern YAP1 contact, while Ser-10, Asp-26 and Lys-715 mediate DGCR8 binding. Collectively, these observations support a working model whereby WBP2 functions as a molecular scaffold to tether YAP1 to the DGCR8 microprocessor complex; this protein-assembly mode has not been previously documented in teleost species. The cornerstone discovery of the current work is that YAP1 is indispensable for WBP2-dependent DGCR8 recruitment to drive miR-133b biogenesis. Cell transfection combined with quantitative real-time PCR demonstrates that knocking down *wbp2* (W0) or *yap1* (Y0) alone markedly reduces pri-miRNA and pre-miRNA abundance and alters mature miR-133b levels. This confirms that both factors are essential for efficient miR-133b maturation. Strikingly, dual-gene knockdown (W0Y0) triggers a synergistic repressive phenotype, which supports their cooperative function within a single regulatory cascade. This distinction is noteworthy, given that the majority of known miRNA-processing modulators (e.g., SMADs, p53) operate without WW-domain-dependent scaffold proteins(Suzuki et al. 2009; Slezak-Prochazka et al. 2010). Furthermore, even though mammalian WBP2 is known to tune miRNA biogenesis via physical contacts with Drosha-DGCR8 (Tabatabaeian et al. 2021b), our study provides the first evidence in teleosts that this regulatory event requires WBP2-YAP1 cooperativity. This finding suggests that this functional cassette is evolutionarily conserved yet has acquired lineage-specific regulatory characteristics.

miRNA expression profiling reveals that target genes from each experimental group exhibit significant enrichment in functional cascades governing hormone biosynthesis, endocrine homeostasis and gonadogenesis. The W0 group displays enrichment for parathyroid hormone production-secretion and calcium-dependent signalling, which orchestrate the endocrine-calcium regulatory axis. The Y0 and W0Y0 groups are enriched in well-characterized sex-steroid-responsive cascades, including MAPK, Hippo and cAMP signaling. The W0Y1 set prioritises insulin and adiponectin-mediated hormonal signaling, whereas the W1Y0 group shows enrichment in GnRH-driven gonadotropin release and cortisol biosynthetic processes. Although the Gper-Src cascade was not individually enriched in our KEGG analysis, downstream effectors including calcium-dependent and MAPK signaling pathways were significantly enriched, implying the potential involvement of rapid oestrogen non-genomic signaling. These signaling nodes have long been functionally tied to estrogen signaling and oocyte maturation. GnRH acts as a central mediator during folliculogenesis by reprogramming gene modules controlling cAMP turnover, ovulatory rhythms and granulosa-cell intercellular contacts(Zhang et al. 2020). In teleost ovaries, estrogen-stimulated cAMP retention sustains the meiotic arrest of oocytes (Das et al. 2017). Rapid non-genomic signaling triggered by the estrogen-ER complex initiates MAPK cascade activation (Marino et al. 2006). Additionally, estrogen-driven Gper-Src signaling mediates EGFR transactivation and enhances Erk1/2 phosphorylation, which maintains meiotic arrest and restrains oocyte maturation in

bony fish (Peyton and Thomas 2011). In murine models, Hippo signaling is functionally coupled to estrogen signaling and ovarian morphogenesis; pathway hyperactivation results in follicle depletion and ovarian underdevelopment (Fu et al. 2023). Collectively, these published reports align closely with our current dataset. The treatment-specific enrichment of hormone-related pathways demonstrates that distinct genetic perturbations reshape the endocrine-sex-steroid signaling network to modulate core physiological events, including gonadal cell proliferation and folliculogenesis in teleosts. This outcome provides candidate regulatory targets for hormone-directed gonadal developmental control. Complementary histomorphological evidence further illustrates that *wbp2* silencing rewires ovarian oocyte dynamics, with a predominant accumulation of primary oocytes. This phenotypic pattern supports a model in which *wbp2* governs estrogen biosynthesis via retrograde modulation of miR-133b.

Pharmacological manipulation demonstrated that exogenous E_2 and tamoxifen markedly remodel the transcript abundance of miR-133b, core estrogen-biosynthesis genes, as well as *wbp2*, *yap1* and *cox2* in cerebral and gonadal tissues, and these molecular responses show obvious tissue- and sex-dependent characteristics. In teleosts, exogenously supplied estradiol remodels gonadal miRNA repertoires and establishes miRNA-governed negative-feedback circuits that restrain aromatase-dependent estrogen overproduction (Cohen and Smith 2014; Wang et al. 2024). Our observations revealed that E_2 elevates miR-133b abundance and suppresses estrogen-biosynthetic transcripts in female gonads, implying an autoregulatory negative-feedback loop whereby estrogen limits its own synthesis via miR-133b. This regulatory paradigm parallels the feedback mechanism characterized in groupers, where E_2 represses specific miRNAs to de-repress *cyp19a1a* expression (Yu et al. 2020). The divergent responsiveness between brain and gonad recapitulates earlier findings: spatially heterogeneous estrogen signalling drives tissue-specific downstream cascades (Chandrasekar et al. 2010). As a selective estrogen receptor modulator (SERM), tamoxifen can interfere with estrogen-dependent transcriptional reprogramming in the gonads of some bony fish (Kitano et al. 2007). In male specimens, tamoxifen induced transcriptional changes distinct from E_2 treatment, substantiating the requirement of estrogen signalling for tuning the *wbp2/yap1*-miR-133b regulatory axis. Importantly, this pharmacological modulation of *wbp2* and *yap1* by E_2/tamoxifen represents an unreported phenotype in teleosts. Nevertheless, these results are only based on correlational pharmacological exposure data and lack definitive genetic functional validation. Future investigations are therefore warranted to elaborate a refined mechanistic model for estrogen-dependent gonadal developmental control.

5. Conclusions

Herein, we systematically investigate the molecular mechanism by which WBP2 and YAP1 synergistically control miR-133b maturation to regulate ovarian development in teleost fish. Combining cell transfection, miRNA sequencing, quantitative real-time PCR, and ovarian histomorphological assays, we demonstrate that co-regulation by WBP2-YAP1 governs the post-transcriptional processing of miR-133b. Meanwhile, miR-133b shows a marked negative correlation with its target transcripts *wbp2* and *yap1*. Ovarian phenotypic evaluation further validates that this regulatory cascade drives oocyte developmental progression. Mechanistically, GST pull-down, XL-MS, and molecular docking confirm direct physical

interactions among WBP2, YAP1 and DGCR8 to form a ternary protein complex. This complex underpins the above-mentioned regulatory circuit. Collectively, our findings reveal that cooperative assembly of the WBP2-YAP1-DGCR8 complex modulates miR-133b biogenesis and thereby mediates ovarian developmental programming in teleosts. Previous work has partially characterized WBP2 as a co-activator of the estrogen receptor (ER) within steroid-dependent signalling cascades. Studies on greater amberjack (*Seriola dumerili*) have reported sex-divergent miR-133b profiles across peripheral blood and the hypothalamic-pituitary-gonadal (HPG) axis. Sexually dimorphic miR-133b levels were negatively correlated with *wbp2* transcript abundance and circulating estrogen titres (Deng et al. 2024). Additional experiments have confirmed the targeting interaction between miR-133b and *wbp2*, as well as the repressive effect exerted by this miRNA (Zhou et al. 2025). Taken together, these results establish a regulatory axis in which miR-133b represses *wbp2* to modulate estrogen biosynthesis during ovarian development. Nevertheless, this single regulatory cascade cannot fully account for the complete underlying regulatory network. Given the known function of oncogenic WBP2 in repressing miRNA maturation downstream of the Hippo signalling pathway, our study identifies a reciprocal regulatory mode in *S. dumerili*. In this mode, *wbp2* controls miR-133b biogenesis via the miRNA-processing machinery. Full experimental validation of this mechanism will complete the bidirectional feedback circuit of the miR-133b-*wbp2*-estrogen-biosynthesis regulatory axis.

Declarations

Acknowledgments

We are grateful to Zhaoqiu Qu and Biao Yuan for assistance with the cell-based experiments.

Author contribution

Jiayu Zhou: Writing-original draft, Investigation, Formal analysis, Data curation; **Qianwen Min:** Investigation, Data curation; **Xin Yi:** Investigation; **Bi Huang:** Supervision, Formal analysis; **Meiqi Lv:** Data curation; **Ruojing Li:** Supervision; **Na Zhao:** Writing-review & editing, Resources, Funding acquisition, Conceptualization; **Bo Zhang:** Writing-review & editing, Supervision, Funding acquisition, Conceptualization.

Funding

This work was funded by the Guangdong High-Level Talent Special Support Program-Young Top-Notch Talent in Science and Technology Innovation(2025TQ09A155), Guangdong Fund Program for Talent Development Support in the East, West and North Regions Project for Marine Ranching Industry 2026R02015 2026R02004 the Talent Special Support of Southern Marine Science and Engineering Guangdong Laboratory (Zhanjiang) (ZJW-2023-01), the Guangdong Basic and Applied Basic Research Foundation (2023A1515010576; 2024A1515012859), and the Open Project Funding of the State Key Laboratory of Marine Aquaculture Breeding and Sustainable Goods (BRESG202504).

Declaration of competing interest

The authors declare that the article is not under consideration for publication elsewhere, and the article's publication is approved by all authors.

Clinical tral number: not applicable

References

1. Abdollahpour H, Jafari Pastaki N, Falahatkar B (2025) Role of 17β-estradiol injection on growth, physiology, and reproductive performance in male goldfish (Carassius auratus) with or without female interaction. Sci Rep 15:33655. https://doi.org/10.1038/s41598-025-17874-6
2. Ba X, Zhuang Z, Zhou Z, et al (2025) Taurine related pathways effect the potential domestication of wild *Larimichthys crocea* adapt to stress environment. Aquaculture 605:742532. https://doi.org/10.1016/j.aquaculture.2025.742532
3. Basu S, Wallner B (2016) DockQ: A Quality Measure for Protein-Protein Docking Models. PLoS ONE 11:e0161879. https://doi.org/10.1371/journal.pone.0161879
4. Bjerga GEK, Williamson AK (2015) Cold shock induction of recombinant Arctic environmental genes. BMC Biotechnol 15:78. https://doi.org/10.1186/s12896-015-0185-1
5. Bornhorst JA, Falke JJ (2000) Purification of proteins using polyhistidine affinity tags. In: Applications of Chimeric Genes and Hybrid Proteins Part A: Gene Expression and Protein Purification. Academic Press, pp 245–254. https://www.sciencedirect.com/science/article/pii/S0076687900260588
6. Boroda A, Privar Y, Maiorova M, et al (2022) Chitosan versus Carboxymethyl Chitosan Cryogels: Bacterial Colonization, Human Embryonic Kidney 293T Cell Culturing and Co-Culturing. International Journal of Molecular Sciences 23:12276. https://doi.org/10.3390/ijms232012276
7. Bose M, Bhattacharyya SN (2016) Target-dependent biogenesis of cognate microRNAs in human cells. Nature Communications 7:12200. https://doi.org/10.1038/ncomms12200
8. Brunelle JL, Green R (2014) Chapter Thirteen - Coomassie Blue Staining. In: Lorsch J (ed) Laboratory Methods in Enzymology: Protein Part C. Academic Press, pp 161–167. https://www.sciencedirect.com/science/article/pii/B9780124201194000136
9. Celie PH, Parret AH, Perrakis A (2016) Recombinant cloning strategies for protein expression. Current Opinion in Structural Biology 38:145–154. https://doi.org/10.1016/j.sbi.2016.06.010
10. Chandrasekar G, Archer A, Gustafsson J-Å, Lendahl MA (2010) Levels of 17β-Estradiol Receptors Expressed in Embryonic and Adult Zebrafish Following In Vivo Treatment of Natural or Synthetic Ligands. PLOS ONE 5:e9678. https://doi.org/10.1371/journal.pone.0009678
11. Chen Y, Zhou W, Li X, et al (2022) Research Progress of Protein-Protein Interaction Based on Liquid Chromatography Mass Spectrometry※. Acta Chimica Sinica 80:817. https://doi.org/10.6023/A22010055

12. Cohen A, Smith Y (2014) Estrogen Regulation of microRNAs, Target Genes, and microRNA Expression Associated with Vitellogenesis in the Zebrafish. Zebrafish 11:462. https://doi.org/10.1089/zeb.2013.0873
13. Dai A, Sun H, Fang T, et al (2013) MicroRNA-133b Stimulates Ovarian Estradiol Synthesis by Targeting Foxl2. FEBS letters 587:2474–2482
14. Dalby B, Cates S, Harris A, et al (2004) Advanced transfection with Lipofectamine 2000 reagent: primary neurons, siRNA, and high-throughput applications. Methods 33:95–103. https://doi.org/10.1016/j.ymeth.2003.11.023
15. Das D, Khan PP, Maitra S (2017) Endocrine and paracrine regulation of meiotic cell cycle progression in teleost oocytes: cAMP at the centre of complex intra-oocyte signalling events. General and Comparative Endocrinology 241:33–40. https://doi.org/10.1016/j.ygcen.2016.01.005
16. Deng Q, Huang Y, Zhao C, et al (2024) Sex-inclined microRNAs in serum exosomes for sex determination in the greater amberjack (*Seriola dumerili*). Aquaculture 587:740886. https://doi.org/10.1016/j.aquaculture.2024.740886
17. Devlin RH, Nagahama Y (2002) Sex determination and sex differentiation in fish: an overview of genetic, physiological, and environmental influences. Aquaculture 208:191–364. https://doi.org/10.1016/S0044-8486(02)00057-1
18. Dhananjayan SC, Ramamoorthy S, Khan OY, et al (2006) WW domain binding protein-2, an E6-associated protein interacting protein, acts as a coactivator of estrogen and progesterone receptors. Molecular Endocrinology 2343–2354. https://doi.org/10.1210/me.2005-0533
19. Fernández-Montero A, Caballero MJ, Torrecillas S, et al (2018) Effect of temperature on growth performance of greater amberjack (*SERIOLA DUMERILI* Risso 1810) Juveniles. Aquac Res 49:908–918. https://doi.org/10.1111/are.13537
20. Fu H, Yang J, Xin B, et al (2023) Accentuated Hippo pathway and elevated miR-132 and miR-195a lead to changes of uteri and ovaries in offspring mice following prenatal exposure to vinclozolin. Reproductive Toxicology 116:108335. https://doi.org/10.1016/j.reprotox.2023.108335
21. Gallagher S, Sasse J (2001) Protein analysis by SDS-PAGE and detection by Coomassie blue or silver staining. Current protocols in pharmacology Appendix 3: https://doi.org/10.1002/0471141755.pha03bs02
22. Hammes SR, Levin ER (2007) Extranuclear Steroid Receptors: Nature and Actions. Endocrine Reviews 726. https://doi.org/10.1210/er.2007-0022
23. Jiang B, Wang L, Fu J, et al (2023) Screening and Identification of Interacting Proteins of Mitfa in Red Tilapia. Fishes 8:241. https://doi.org/10.3390/fishes8050241
24. Jiang P, Ren L, Zhi L, et al (2021) Protocol for cell preparation and gene delivery in HEK293T and C2C12 cells. STAR Protocols 2:. https://doi.org/10.1016/j.xpro.2021.100497
25. Jo MJ, Nam HJ (2025) Protocol to screen chemicals to enhance homology-directed repair in CRISPR-Cas9 gene editing. STAR Protoc 6:103896. https://doi.org/10.1016/j.xpro.2025.103896

26. Jones AX, Cao Y, Tang Y-L, et al (2019) Improving mass spectrometry analysis of protein structures with arginine-selective chemical cross-linkers. Nat Commun 10:3911. https://doi.org/10.1038/s41467-019-11917-z
27. Kim S-Y, Hakoshima T (2019) GST Pull-Down Assay to Measure Complex Formations. In: The Hippo Pathway. Humana Press, New York, NY, pp 273–280. https://link.springer.com/protocol/10.1007/978-1-4939-8910-2_20
28. Kitano T, Yoshinaga N, Shiraishi E, et al (2007) Tamoxifen induces masculinization of genetic females and regulates P450 aromatase and müllerian inhibiting substance mRNA expression in Japanese flounder (Paralichthys olivaceus). Molecular Reproduction and Development 74:1171–1177. https://doi.org/10.1002/mrd.20603
29. Lanio T, Jeltsch A, Pingoud A (2003) High-Throughput Purification of PolyHis-Tagged Recombinant Fusion Proteins. In: E. coliGene Expression Protocols. Humana Press, pp 199–204. https://link.springer.com/protocol/10.1385/1-59259-301-1:199
30. Li L, Trent JC, Eid JE (2023) Optimized lentiviral vector transduction of adherent cells and analysis in sulforhodamine B proliferation and chromatin immunoprecipitation assays. STAR Protocols 4:. https://doi.org/10.1016/j.xpro.2023.102109
31. Li R-J, Zhuang Z-J, Qu Z-Q, et al (2025) Host immune constraints delineate the window of microbial colonization during early development of *Larimichthys crocea*. zr 47:17–31. https://doi.org/10.24272/j.issn.2095-8137.2025.258
32. Liu X, Wei J, Ma Z, He Y (2019) Rapamycin- and starvation-induced autophagy are associated with miRNA dysregulation in A549 cells. Acta Biochim Biophys Sin (Shanghai) 51:393–401. https://doi.org/10.1093/abbs/gmz022
33. Livak KJ, Schmittgen TD (2001) Analysis of Relative Gene Expression Data Using Real-Time Quantitative PCR and the 2 – ΔΔCT Method. Methods 25:402–408. https://doi.org/10.1006/meth.2001.1262
34. Louche A, Salcedo SP, Bigot S (2017) Protein–Protein Interactions: Pull-Down Assays. In: Bacterial Protein Secretion Systems. Humana Press, New York, NY, pp 247–255. https://doi.org/10.1007/978-1-4939-7033-9_20
35. Ma Z, Yang J, Zhang Q, et al (2021) miR-133b targets tagln2 and functions in tilapia oogenesis. Comparative Biochemistry and Physiology Part B Biochemistry and Molecular Biology 256:110637. https://doi.org/10.1016/j.cbpb.2021.110637
36. Marino M, Galluzzo P, Ascenzi P (2006) Estrogen Signaling Multiple Pathways to Impact Gene Transcription. Current Genomics 7:497–508. https://doi.org/10.2174/138920206779315737
37. Mori M, Triboulet R, Mohseni M, et al (2014) Hippo Signaling Regulates Microprocessor and Links Cell-Density-Dependent miRNA Biogenesis to Cancer. Cell 156:893–906. Https://doi.org/10.1016/j.cell.2013.12.043
38. Nettleship JE, Rada H, Owens RJ (2019) Overview of a High-Throughput Pipeline for Streamlining the Production of Recombinant Proteins. In: High-Throughput Protein Production and Purification.

Humana, New York, NY, pp 33–49. https://link.springer.com/protocol/10.1007/978-1-4939-9624-7_2

39. Nicol B, Estermann M, Yao H, Mellouk N (2022) Becoming female: Ovarian differentiation from an evolutionary perspective. Frontiers in Cell and Developmental Biology 10. https://doi.org/10.3389/fcell.2022.944776
40. Pan M, Liu J, Huang D, et al (2021) FoxO3 Modulates LPS-Activated Hepatic Inflammation in Turbot (Scophthalmus maximus L.). Frontiers in Immunology 12. https://doi.org/10.3389/fimmu.2021.679704
41. Peyton C, Thomas P (2011) Involvement of Epidermal Growth Factor Receptor Signaling in Estrogen Inhibition of Oocyte Maturation Mediated Through the G Protein-Coupled Estrogen Receptor (Gper) in Zebrafish (Danio rerio). Biology of Reproduction 85:42. https://doi.org/10.1095/biolreprod.110.088765
42. Presslauer C, Tilahun Bizuayehu T, Kopp M, et al (2017) Dynamics of miRNA transcriptome during gonadal development of zebrafish. Sci Rep 7:43850. https://doi.org/10.1038/srep43850
43. Qu Z, Zhou J, Li R, et al (2025) Integrated transcriptomic and microbiota analyses reveal growth-related intestinal responses to feeding strategies in Nibea coibor. Adv Biotechnol 3:37. https://doi.org/10.1007/s44307-025-00088-2
44. Slezak-Prochazka I, Durmus S, Kroesen B-J, Berg A van den (2010) MicroRNAs, macrocontrol: Regulation of miRNA processing. RNA 16:1087–1095. https://doi.org/10.1261/rna.1804410
45. Smith DB, Johnson KS (1988) Single-step purification of polypeptides expressed in *Escherichia coli* as fusions with glutathione *S*-transferase. Gene 67:31–40. https://doi.org/10.1016/0378-1119(88)90005-4
46. Sohn M-Y, Kang G, Kim K-H, et al (2025) Functional Characterization of TNFα in the Starry Flounder (Platichthys stellatus) and Its Potential as an Immunostimulant. Animals 15:2119. https://doi.org/10.3390/ani15142119
47. Sudol M, Henry I. Chen, Bougeret C, et al (1995) Minireview Characterization of a novel protein-binding module - the WW domain. FEBS Letters 369: 67–71. https://doi.org/10.1016/0014-5793(95)00550-S
48. Supratim Dey, Saurabh Gireesan, Solovou T, et al (2025) High-Throughput Pipeline for Protein Expression and Solubility Profiling Using Synthetically Generated Plasmids. https://doi.org/10.1002/cpz1.70188
49. Suzuki HI, Yamagata K, Sugimoto K, et al (2009) Modulation of microRNA processing by p53. Nature 460:529–533. https://doi.org/10.1038/nature08199
50. Tabatabaeian H, Lim SK, Chu T, et al (2021a) WBP2 inhibits microRNA biogenesis via interaction with the microprocessor complex. Life Science Alliance 4:e202101038. https://doi.org/10.26508/lsa.202101038
51. Tabatabaeian H, Lim SK, Chu T, et al (2021b) WBP2 inhibits microRNA biogenesis via interaction with the microprocessor complex. Life Science Alliance 4:e202101038. https://doi.org/10.26508/lsa.202101038

52. Tabatabaeian H, Rao A, Ramos A, et al (2020) The emerging roles of WBP2 oncogene in human cancers. Oncogene. https://doi.org/10.1038/s41388-020-1318-0
53. Thong B, Soldin Sj, Lingwood Ca (1985) Lack of specificity of current anti-digoxin antibodies, and preparation of a new, specific polyclonal antibody that recognizes the carbohydrate moiety of digoxin. Clinical chemistry 10:1625. https://pubmed.ncbi.nlm.nih.gov/4042328/
54. Tunyasuvunakool K, Adler J, Wu Z, et al (2021) Highly accurate protein structure prediction for the human proteome. Nature 596:590–596. https://doi.org/10.1038/s41586-021-03828-1
55. Wang DS, Kobayashi T, Zhou LY, et al (2007) Foxl2 up-regulates aromatase gene transcription in a female-specific manner by binding to the promoter as well as interacting with ad4 binding protein/steroidogenic factor 1. Molecular Endocrinology 712
56. Wang J-H, Tang Y-L, Gong Z, et al (2022) Characterization of protein unfolding by fast cross-linking mass spectrometry using di-ortho-phthalaldehyde cross-linkers. Nat Commun 13:1468. https://doi.org/10.1038/s41467-022-28879-4
57. Wang Y, Yang F, Liu S, et al (2024) Coordinated regulatory feedback between estradiol and miR-17-92 cluster in ovaries of Japanese flounder *Paralichthys olivaceus*. Aquaculture 589:740975. https://doi.org/10.1016/j.aquaculture.2024.740975
58. Yamaguchi T, Yamaguchi S, Hirai T, Kitano T (2007) Follicle-stimulating hormone signaling and Foxl2 are involved in transcriptional regulation of aromatase gene during gonadal sex differentiation in Japanese flounder, Paralichthys olivaceus. Biochem Biophys Res Commun 359:935–940 https://doi.org/10.1016/j.bbrc.2007.05.208
59. Yan Y, Tao Y, Cao Z, et al (2022) The Effect of Knocked-Down Anti-Müllerian Hormone mRNA on Reproductive Characters of Male Nile Tilapia (Oreochromis niloticus) through Inhibition of the TGF-Beta Signaling Pathway. Fishes 7:299. https://doi.org/10.3390/fishes7050299
60. Yang Xh, Wu Yz, Xiao K, et al (2020) Preparation of PrP-specific Polyclonal Antibody via Immunization of PRNP-knockout Mice with Recombinant Human PrP Protein. Biomedical and environmental sciences: BES 33:. https://doi.org/10.3967/bes2020.066
61. Yin Y, Zhang Z, Gou Y, et al (2026) Transcriptome Sequencing of LYPLA1 Gene Overexpression and Interference. Animals 16:2648. https://doi.org/10.3390/ani16172648
62. Yu D, Chojnowski G, Rosenthal M, Kosinski J (2023) AlphaPulldown—a python package for protein–protein interaction screens using AlphaFold-Multimer. Bioinformatics 39:. https://doi.org/10.1093/bioinformatics/btac749
63. Yu Q, Peng C, Ye Z, et al (2020) An estradiol-17β/miRNA-26a/*cyp19a1a* regulatory feedback loop in the protogynous hermaphroditic fish, *Epinephelus coioides*. Molecular and Cellular Endocrinology 504:110689. https://doi.org/10.1016/j.mce.2019.110689
64. Zhang K, Gao G, Zhao X, et al (2020) The direct effects of gonadotropin-releasing hormone on proliferation of granulosa cells and development of follicles in goose. Br Poult Sci 61:242–250. https://doi.org/10.1080/00071668.2020.1724877

65. Zhang X, Li M, Ma H, et al (2017) Mutation of foxl2 or cyp19a1a Results in Female to Male Sex Reversal in XX Nile Tilapia. Endocrinology 8: 2634. https://dx.doi.org/10.1210/en.2017-00127
66. Zhang Y, Wang X, Gao Z, et al (2024) Hypoxia-inducible factor-1α promotes macrophage functional activities in protecting hypoxia-tolerant large yellow croaker (Larimichthys crocea) against Aeromonas hydrophila infection. Front Immunol 15:1410082. https://doi.org/10.3389/fimmu.2024.1410082
67. Zhao N, He X, Min Q, et al (2025) Sex-biased miR-456 targeting spire1/sox11 provides insights into the ceRNA-network of sexual regulation in fish. Water Biology and Security 4:100370. https://doi.org/10.1016/j.watbs.2025.100370
68. Zhao N, Jia L, He X, Zhang B (2021) Sex bias miRNAs in *Cynoglossus semilaevis* could play a role in transgenerational inheritance. Comparative Biochemistry and Physiology Part D: Genomics and Proteomics 39:100853. https://doi.org/10.1016/j.cbd.2021.100853
69. Zhao N, Wang Q, Deng Q, et al (2023) Heterogeneity of sex-biased miRNAs profiling of *Cynoglossus semilaevis* between exosome and sperm. Aquaculture 563:738898. https://doi.org/10.1016/j.aquaculture.2022.738898
70. Zhou J, Min Q, Ba X, et al (2025) miR-133b regulation of wbp2 in ovaries is conserved among teleosts. Acta Oceanologica Sinica 44:189–200. https://doi.org/10.1007/s13131-025-2560-7
71. Zhu L, Wang X, Yuan P, Wang G (2021) [Preparation and identification of rat anti-human ErbB3 dimerization domain polyclonal antibody]. Xi bao yu fen zi mian yi xue za zhi = Chinese journal of cellular and molecular immunology 37 6: 551–556. https://pubmed.ncbi.nlm.nih.gov/34060450/
72. Zohar Y (2021) Fish reproductive biology – Reflecting on five decades of fundamental and translational research. General and Comparative Endocrinology 300:113544. https://doi.org/10.1016/j.ygcen.2020.113544

Figures

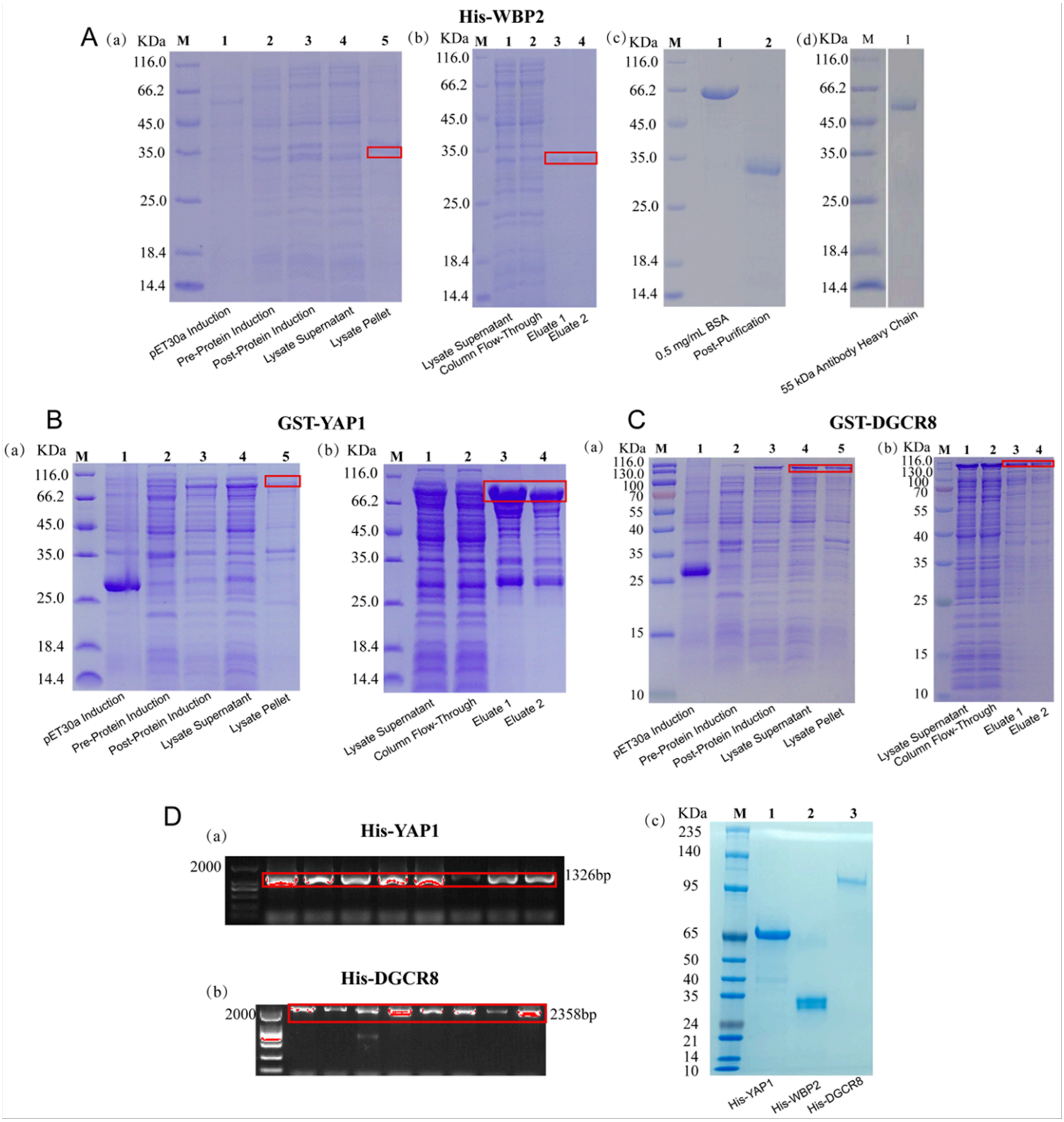


Figure 1

Production, purification and immunological characterization of recombinant WBP2, YAP1 and DGCR8 proteins

(A) Expression, purification and immunoblot validation of His-WBP2. a, SDS-PAGE analysis of bacterial lysates with or without IPTG induction; b, SDS-PAGE profile of affinity-purified protein; c, SDS-PAGE

assessment of protein purity; d, immunoblotting-based antibody verification. (B) Inducible expression and purification of GST-YAP1. a, SDS-PAGE analysis of samples collected pre- and post-induction; b, SDS-PAGE of the purified recombinant product. (C) Inducible expression and purification of GST-DGCR8. a, SDS-PAGE analysis of samples collected pre- and post-induction; b, SDS-PAGE of the purified recombinant product. (D) Recombinant plasmid validation and overview of purified recombinant proteins. a and b, agarose gel electrophoresis for the identification of pET-His-YAP1 and pET-His-DGCR8 constructs, respectively; c, SDS-PAGE of purified His-YAP1, His-WBP2 and His-DGCR8 proteins.

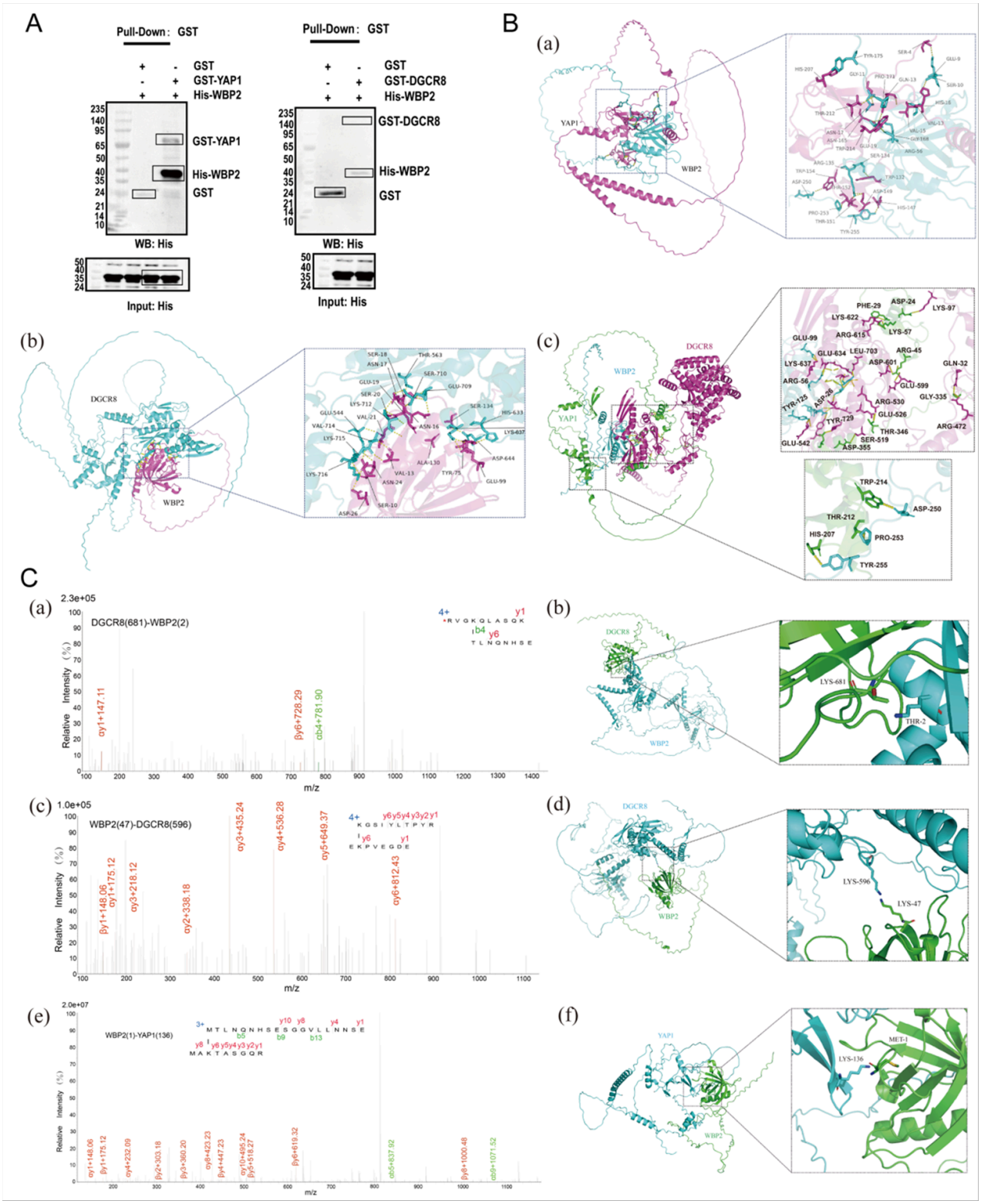


Figure 2

Biochemical validation, molecular docking and CX-MS characterization of WBP2-YAP1-DGCR8 protein interactome

(A) In *vitro* GST pull-down assays were conducted to interrogate physical interactions between His-WBP2 and recombinant GST-YAP1/GST-DGCR8. The upper blot displays immunodetection of pull-down eluates with an anti-His antibody, whereas the lower blot corresponds to total protein input controls. (B) Molecular docking simulations predicted pairwise binding architectures for WBP2-YAP1 and WBP2-DGCR8, alongside the spatial assembly of the ternary complex. (a) Predicted binding interface of the WBP2-YAP1 dimer; (b) Predicted binding interface of the WBP2-DGCR8 dimer; (c) Contact surface of the WBP2-YAP1-DGCR8 ternary complex. Insets on the right highlight hydrogen-bond networks formed at critical amino-acid residues. (C) Chemical cross-linking mass spectrometry (CX-MS) mapped intermolecular contact sites across the protein assembly. (a, c, e) Representative mass spectra for cross-linked peptides of DGCR8-WBP2, WBP2-DGCR8 and WBP2-YAP1, with diagnostic fragment ions and cross-linked peptide sequences labelled; (b, d, f) Three-dimensional interaction models reconstructed from CX-MS cross-linking restraints, with magnified views denoting the spatial coordinates of core cross-linkable lysine (Lys) residues.

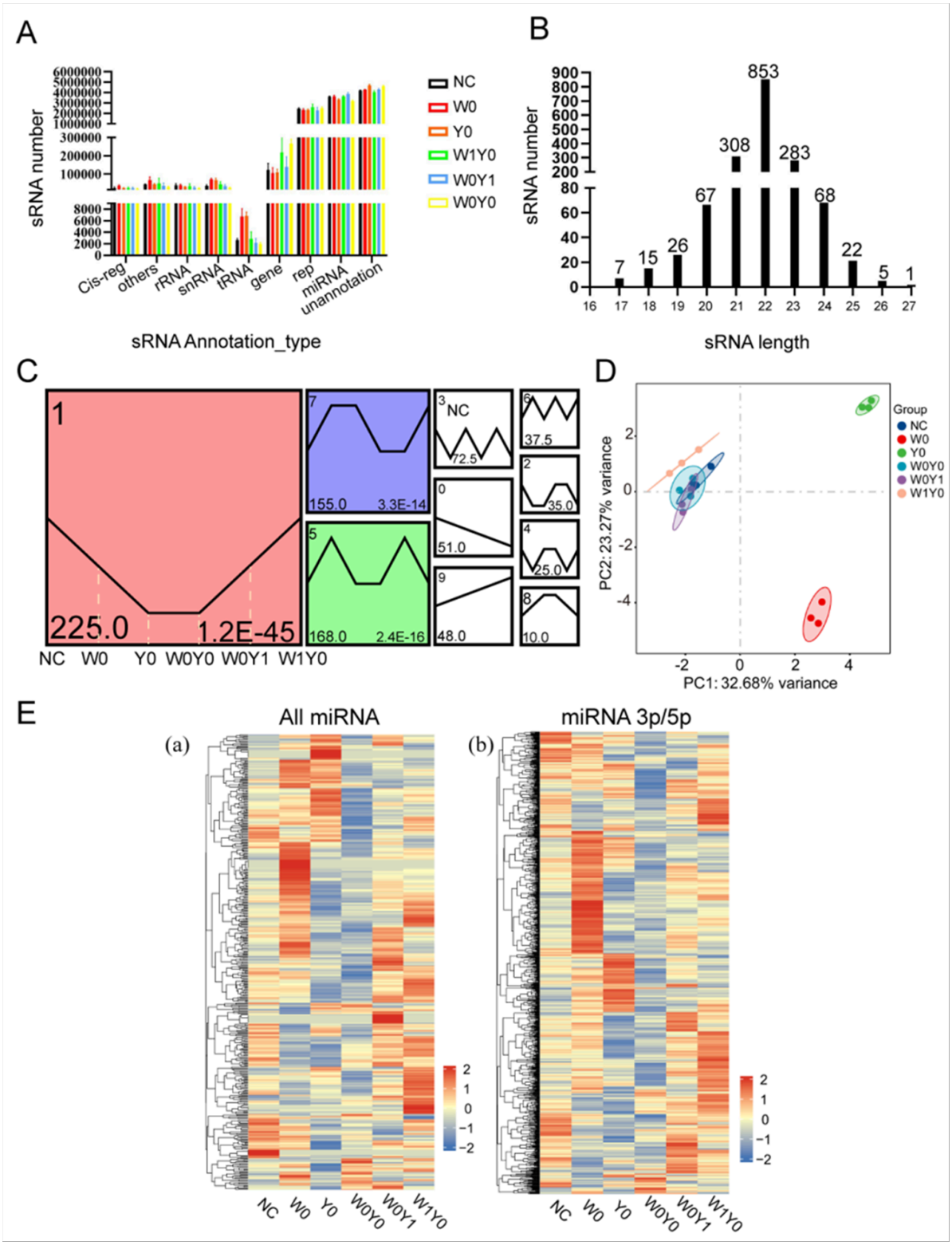


Figure 3

Small-RNA-seq quality control and miRNA expression profiling

(A) Classification statistics of annotated sRNA biotypes among experimental groups. The x-axis lists sRNA annotation biotypes, while the y-axis quantifies read counts allocated to each category. Colour coding distinguishes treatments (NC: negative control; W0, Y0, W0Y0, W1Y0, W1Y1: test groups). (B)

Size-distribution profiling of sRNA reads. The x-axis denotes nucleotide length (nt), and the y-axis represents the abundance of reads at each size. (C) Short Time-series Expression Miner (STEM) analysis for temporal trends of differentially expressed miRNAs. Statistically significant expression modules (Module 1, 5, 7, etc.) were identified across six experimental contexts. Each module is annotated with miRNA count and the corresponding significance *p*-value. (D) Principal-component-analysis (PCA) scatter plot derived from miRNA expression matrices. PC1 and PC2 account for 32.68% and 23.27% of the overall transcriptional variance, respectively. Colours discriminate independent experimental treatments. (E) Hierarchical-clustering heatmaps depicting the expression architecture of differentially expressed miRNAs. (a) Global clustering heatmap covering the full miRNA repertoire; (b) Strand-resolved heatmap discriminating 5p- and 3p-derived miRNA isoforms. The colour scale denotes normalised read abundance, with red indicating high expression and blue indicating low expression. Rows and columns correspond to miRNAs and biological samples, respectively. Dendrograms recapitulate pairwise expression relatedness for both miRNAs and specimens.

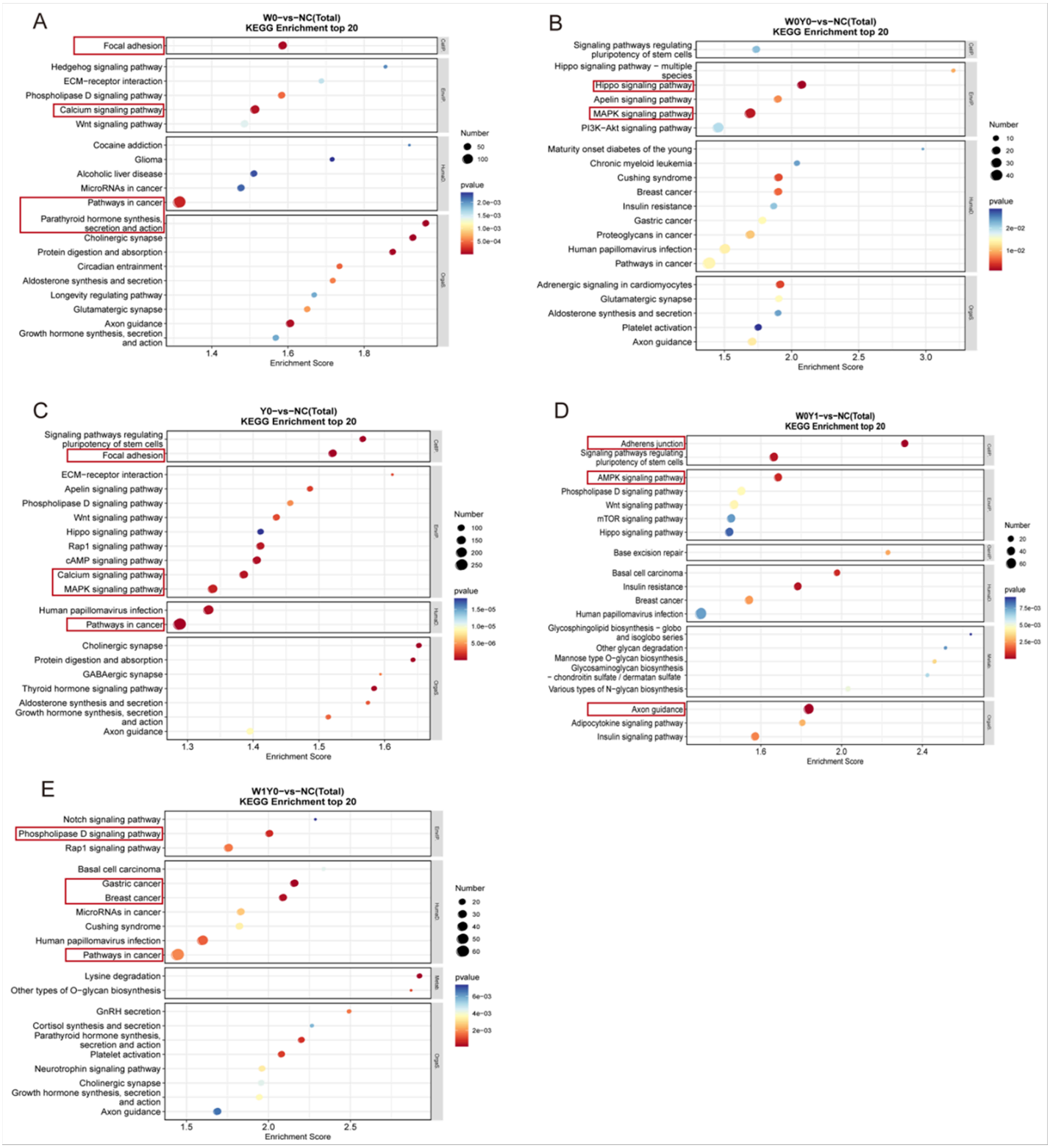


Figure 4

Bubble plots illustrating KEGG pathway enrichment for target genes of differentially expressed miRNAs across experimental treatments

(A) NC, negative control；W0 vs NC; (B) W0Y0 vs NC; (C) Y0 vs NC; (D) W0Y1 vs NC; (E) W1Y0 vs NC. Bubble size denotes the count of target genes assigned to each enriched pathway. The colour scale

maps to enrichment significance, where red colour corresponds to lower *p*-values and more robust enrichment. The x-axis represents the enrichment score, while the y-axis displays individual KEGG pathway terms. Red rectangles highlight the key differentially modulated pathways for each comparison.

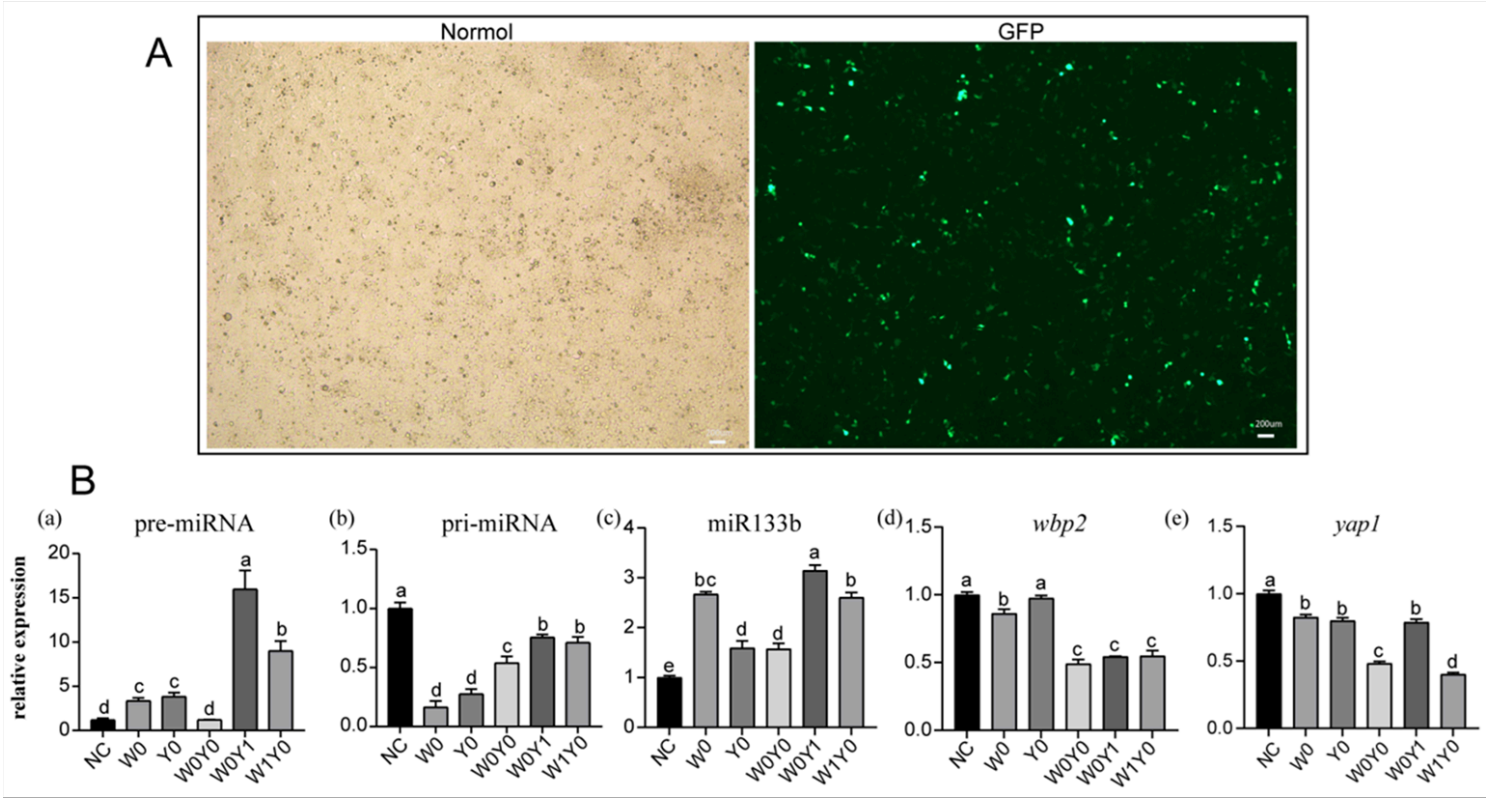


Figure 5

Validation of transfection efficiency in gonadal cells and qRT-PCR-based expression analysis of core regulatory genes

(A) Representative micrographs demonstrating cell transfection efficiency under bright-field (Normal) and GFP fluorescence illumination. Scale bar, 200 μm. (B) Relative transcript abundance of pre-miRNA, pri-miRNA, mature miR-133b, and its target genes wbp2 and yap1 across experimental treatments. Statistically significant differences among groups are denoted by distinct lowercase letters ($p < 0.05$). The data represent the mean ± standard deviation (n=3). NC, control group; W0, Y0, W0Y0, W0Y1, W1Y0, various experimental treatments.

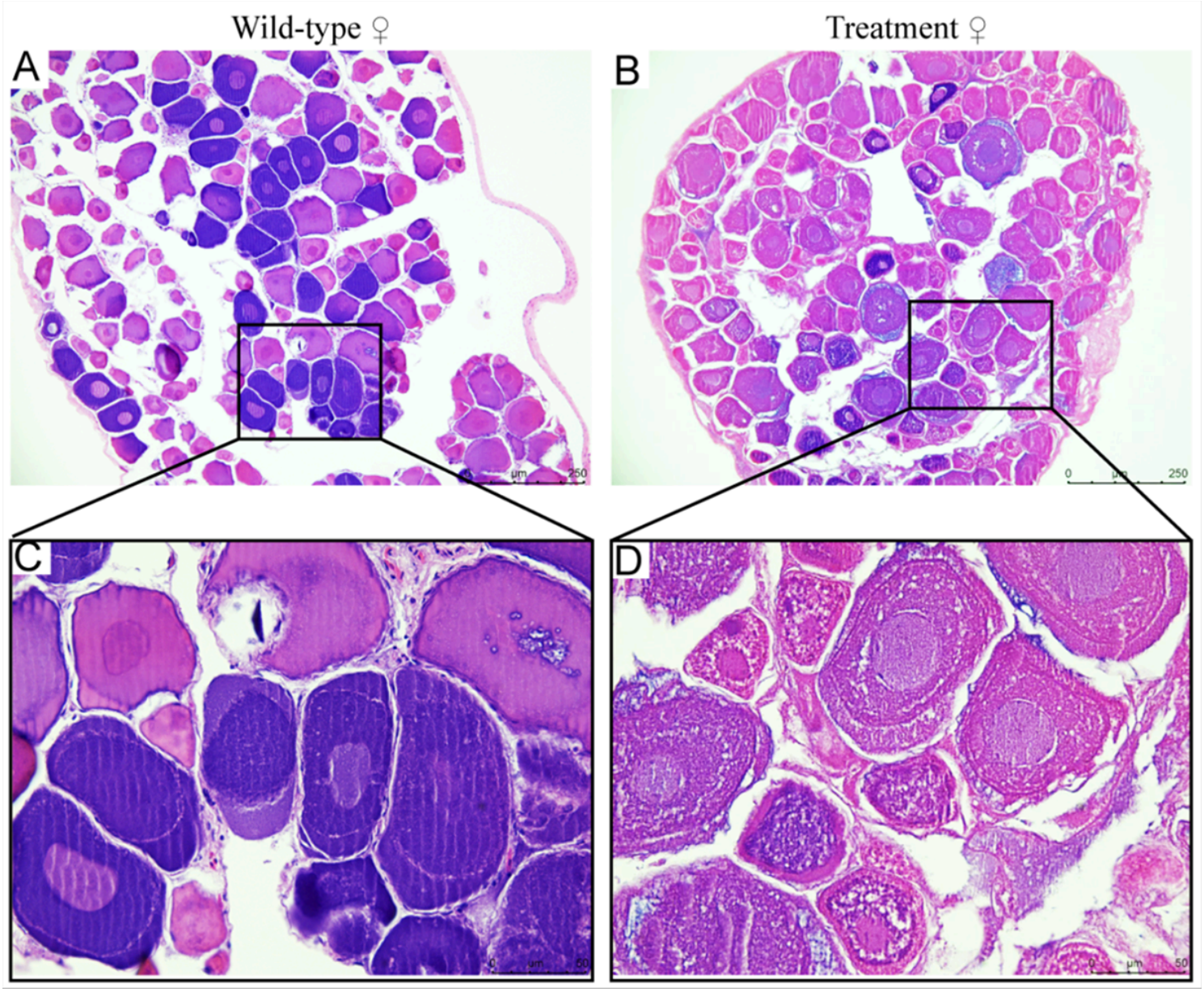


Figure 6

Histomorphological comparison of ovaries from wild-type and siRNA-treated female individuals

(A, C) Micrographs of ovarian sections from wild-type females (Wild-type ♀) at low and high magnification. (B, D) Micrographs of ovarian sections from siRNA-treated females (Treatment ♀) at low and high magnification. Scale bars, 250 μm (A, B); scale bars, 100 μm (C, D).

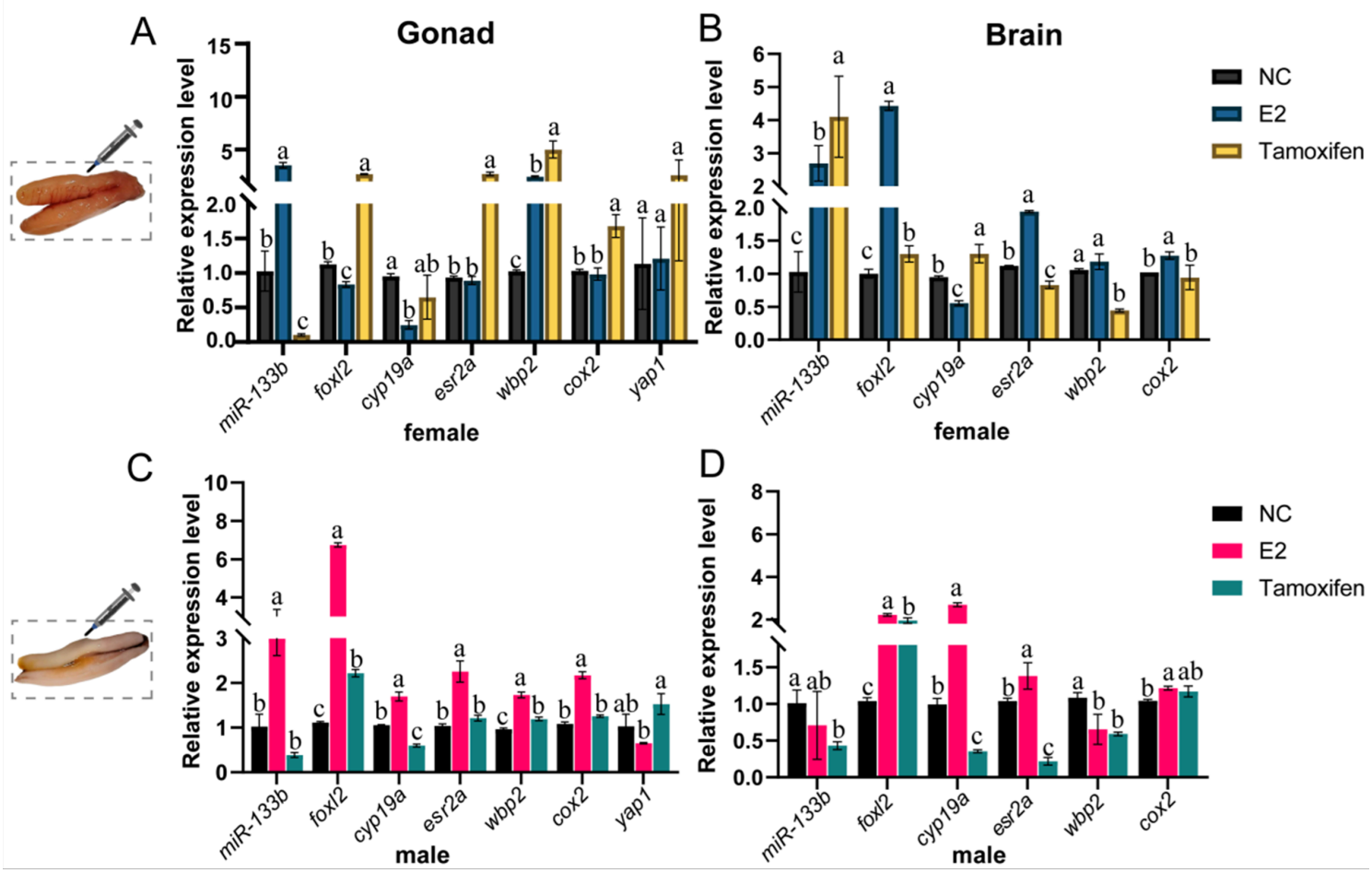


Figure 7

Relative transcript abundances of genes involved in estrogen biosynthesis and signalling pathways in the gonad and brain of female and male individuals following 17β-estradiol (E2) and tamoxifen exposure.

(A) Female gonad; (B) Female brain; (C) Male gonad; (D) Male brain. NC, corn-oil solvent control; E2, 17β-estradiol-treated group; Tamoxifen, tamoxifen-treated group. The y-axis denotes relative gene expression. Distinct lowercase letters denote statistically significant differences among treatments ($p < 0.05$). The data represent the mean ± standard deviation (n=3). Assayed molecules comprised miR-133b, *foxl2*, *cyp19a*, *esr2a*, *wbp2*, *cox2*, and *yap1*.

Supplementary Files

This is a list of supplementary files associated with this preprint. Click to download.

- Table1.doc